Journal of Colloid and Interface Science 576 (2020) 322–329

Contents lists available at ScienceDirect

Journal of Colloid and Interface Science

journal homepage: www.elsevier.com/locate/jcis

Spherical probes for simultaneous measurement of rotational and translational diffusion in 3 dimensions

Beybin Ilhan *, Jelle J. Schoppink, Frieder Mugele, Michael H.G. Duits

Physics of Complex Fluids Group and MESA+ Institute, Faculty of Science and Technology, University of Twente, PO Box 217, 7500 AE Enschede, the Netherlands

GRAPHICAL ABSTRACT

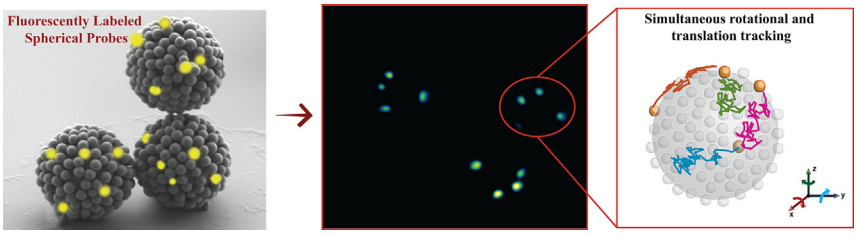

ARTICLE INFO

Article history:
Received 17 March 2020
Revised 17 April 2020
Accepted 8 May 2020
Available online 13 May 2020

Keywords:
3 dimensional
Rotational diffusion
Colloidal spheres
Single particle tracking
Raspberry colloids
Rotational probes
Confocal scanning laser microscopy

ABSTRACT

Real time visualization and tracking of colloidal particles with 3D resolution is essential for probing the local structure and dynamics in complex fluids. Although tracking translational motion of spherical particles is well-known, accessing rotational dynamics of such particles remains a great challenge. Here, we report a novel approach of using fluorescently labeled raspberry-like colloids with an optical anisotropy to concurrently track translational and rotational dynamics in 3 dimensions. The raspberry-like particles are coated by a silica layer of adjustable thickness, which allows tuning the surface roughness. The synthesis and applicability of the proposed method is demonstrated by two types of probes: rough and smoothened. The accuracies of measuring Mean Squared (Angular) Displacements are also demonstrated by using these 2 probes dispersed in 2 different solvents. The presented 3D trackable colloids offer a high potential for wide range of applications and studies, such as probing the dynamics of crystallization, phase transitions, biological interactions and the effect of surface roughness on diffusion.

1. Introduction

Studying colloidal dynamics via time-resolved locations of individual particles can provide microscopic insight into a variety of physical phenomena in different phases of matter [1–5]. Especially in systems with an intrinsic inhomogeneity, correlating the dynamics with the location inside the material can provide unique information that cannot be obtained with techniques that take an ensemble average over all particles, or any other bulk method. Examples of research areas where local translational dynamics have been analyzed for this purpose include dense suspensions [6], glassy materials [7–9], polymer networks [10,11], spatially confined materials [12–15], food products [16], cell biology [17,18] and virus infection mechanisms [19].

In contrast to the many studies on translational dynamics, research related to rotational dynamics is rather scarce. This has been ascribed to a lack of experimental approaches for capturing rotational motion [20]. Rotational dynamics can shed a unique light onto various dynamic phenomena that cannot be accessed only with translational degrees of freedom, such as motion in glassy and supercooled states (where decoupling between translational and rotational diffusion emerges) [21–23]; particle adsorption and self-assembly at fluid interfaces [24,25]; interfacial

* Corresponding author.
E-mail address: b.ilhan@utwente.nl (B. Ilhan).

https://doi.org/10.1016/j.jcis.2020.05.026
0021-9797/

dynamics at solid-liquid interfaces [26] and biological interactions; such as viruses binding to membranes [27].

Ensemble averaged rotational diffusion of colloids has been studied by techniques such as fluorescence recovery after photobleaching (FRAP) [28,29], depolarized dynamic light scattering [30] and nuclear magnetic resonance (NMR) spectroscopy [31]. These bulk methods fall short in identifying local (dynamic) heterogeneities. Measuring rotational diffusion via individual probe particles can provide valuable local information in terms of dynamic length scales and structural signatures of complex fluids, such as local defects and crosslink densities in polymer networks [32], local rheology of soft materials [33], or intrinsic features of active fluids in biochemical processes [34].

In recent years, different strategies have been used towards tracking the rotational motion of diffusive probes of both spherical and anisotropic particle shapes such as rods, ellipsoids, and particle clusters [35–39]. Here, geometrical anisotropy is widely utilized because it naturally provides an identifiable optical axis to track angular displacements [20]. For spherical colloids, the lack of such a natural frame of reference requires a design where the optical isotropy is broken. A common type of such probes is the modulated optical nanoprobes (MOON) [40,41]. This type of Janus particle usually consists of a fluorescent sphere that is half coated with a metal layer. Although these rotational probes are attracting interest in various fields [42], they have some drawbacks too. Due to the metal coating on one side, the surface chemistry is no longer uniform, and refractive index mismatches with the surrounding medium may compromise the image quality, especially for biological systems and high volume concentrations. Recently a new type of spherical shaped rotational probes was introduced [23,43]. These probes are bicolor or multicolor colloidal spheres with an eccentric core(s) shell structure, requiring multiple excitation wavelengths to be used. Although they provide homogenous surface chemistry, the centers of the core and the shell may not coincide precisely. In the case where connected cores with different labels are utilized, they have to be overgrown to a rather large size, to attain a (near) spherical overall shape.

In this work, we introduce a simple method for i) synthesizing fluorescently labelled raspberry-like spherical probes and ii) using them for simultaneously accessing rotational and translational dynamics in 3D. Our probes are made by densely covering a large silica (SiO_2) core with many small SiO_2 particles, a fraction of which is fluorescently labeled. By coating these raspberries with a layer of silica of controllable thickness, we obtain particles of variable roughness while maintaining uniform surface chemistry. The optical anisotropy, introduced via the fluorescent tracers, allows for simultaneous tracking of the translational and rotational motion of each probe in 3D, using just one fluorescent dye. We demonstrate a proof of concept by tracking 2 types of probes (smoothened and rough) in the dilute regime, and measuring the Mean Squared (Angular) Displacements.

2. Material and methods

2.1. Materials

TetraEthoxySilane, 25 wt% Ammonia, analytical grade ethanol (99.9%, Emsol), 0.1 N nitric acid solution (HNO_3), anhydrous dimethyl sulfoxide (>99.9%) and glycerol (99.5%) are purchased from Sigma Aldrich. All purchased chemicals are used as received. Deionized water (resistivity: 18 MΩ cm^{-1}) is obtained from a Millipore Synergy instrument. Core SiO_2 particles (r = 1.06 μm) with amine (NH_2) surface modification are purchased from Microparticles GmbH. Two types of smaller SiO_2 particles (berries) are used: fluorescent particles, (sicastar-greenF, plain, r = 0.15 μm) are purchased from Micromod Partikeltechnologie GmbH, while plain SiO_2 particles are synthesized via the Stöber method [44,45].

2.2. Synthesis of fluorescently labelled raspberries

Raspberry particles are synthesized by coating the surface of positively functionalized (–NH2) SiO_2 spheres (*core*, r = 1.04 ± 0.0 33 μm) with a dense layer of negatively charged small SiO2 spheres (*berry*, r = 0.160 ± 0.014 μm) via electrostatic heteroaggregation [46]. While the presence of (+) amine groups on the cores, and (-) silanol ones on the berries already favors such aggregation, an optimization of the pH is needed to obtain interparticle bonds that are strong enough to prevent detachment by stirring forces. Meanwhile, also the stability (against homo-aggregation) has to be preserved for both cores and berries. Using HNO_3 to adjust the pH, Zeta potential measurements are conducted at varying pH for the aqueous dispersions of the particles. The results (shown in SI Fig. S1) indicate an optimal pH of 4.5, where, ζ_{core} = +31 mV and ζ_{berry} = −28 mV, $\zeta_{fluo.berry}$ = −21 mV.

Besides the zeta potentials, also the mixing ratio of the cores and berries has to be considered. The number of berry particles needed to ensure dense coverage on a core particle is estimated by calculating how many berry particles can be fitted into the shell space between a hypothetical sphere with a radius of [R_{core} + 2-R_{berry}] and a core particle. For our system, this calculation gives 386 berries per core. In practice more berries are needed to ensure colloidal stability throughout the self-assembly process. Especially at the initial stages where the cores are only partially covered by berries, 'bridging aggregation' (berries binding to two cores) must be avoided. To prevent this, a 10 times higher dose of berries is used.

To obtain optical anisotropy, a mixture of equally sized plain and fluorescent berries is used (see Fig. 1a), with a mixing ratio that typically leads to 4–5 fluorescent berries per particle. Assuming that all berries have an equal probability of being bonded to a core surface, the proportion of fluorescent berries is chosen to be ~1.0%. The hetero-aggregation is achieved by adding cores to a suspension of berry particles (~1% wt) under mild stirring, and giving a reaction time of 1 h. Excess berries are removed by 3 cycles of gravity settling and redispersion in aqueous solution at pH 4.5.

To preserve mechanical integrity and to modify the surface roughness, a silica layer is overgrown on to these colloids via seeded growth [47]. Fig. 1b and 1c show confocal fluorescence images of typical probes without/with fluorescent berries. Fig. 1d and 1e show SEM and TEM images for 2 systems differing in the layer thickness and hence in final size (they are identical otherwise): Surface rough probes (RP) with an rms roughness of 58 nm (4.5% relative to average raspberry radius) and Smoothened probes (SP) with 23 nm rms (1.5% relative).

2.3. Characterization methods

The hydrodynamic radii of the two berry systems, as measured with Dynamic Light Scattering (Malvern Zetasizer Nano ZS), are used to obtain equal sizes via seeded growth on the plain silica [48]. The size distributions of the cores, berries and probes are measured from TEM images (Philips CM300ST-FEG, 300 kV). Radii are measured from the fitted largest Feret diameter (ImageJ, FIJI). Core and berry size distributions are shown in SI Fig. S2. SEM images are obtained with a Zeiss MERLIN HR-SEM. The mass den-

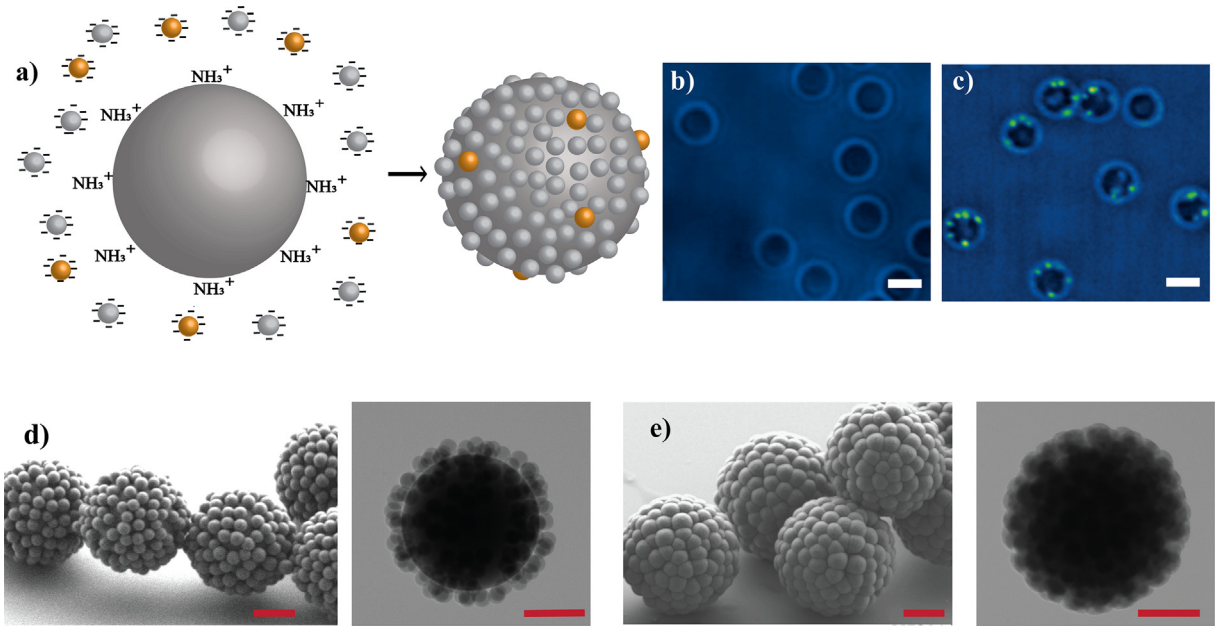

Fig. 1. (a) Illustration of the synthesis of the probe raspberries. (b, c) Superimposed brightfield and fluorescence images of raspberry probes without/with fluorescent berries (white scale bars are 2 μm). A movie of their Brownian motion can be seen in the Supporting Information as S.mov1. (d, e) SEM and TEM images of rough (RP) and smoothened probes (SP) (red scale bars are 1 μm).

sity of the raspberry particles are measured with pycnometry and found to be 1.62 ± 0.06 g/cm^3.

The surface coverage of the berries on the raspberries is characterized with atomic force microscopy (AFM), (Dimension Icon, Bruker). Samples are analyzed in air using cantilevers from Mikro Masch, NSC36 with a spring constant of 0.6 N/m and a sharp Si tip (R_{tip} < 10 nm). Surface roughness is quantified by calculation of root-mean-square (RMS) amplitude from AFM height profiles. The apical zones of individual particles are fitted with a sphere via least squares regression by a custom made Matlab program. Subsequently, the radial component of the spherical fit is subtracted from the distance between the center of the smooth profile and each (x,y,z) surface location[49]. Details of this characterization can be found in SI Fig. S6.

2.4. Confocal microscopy experiments

Raspberry particles are dispersed in refractive index matching solvents (S_1 or S_2), starting from the water-based stock suspensions, and using the known mass densities to calculate the mixing ratios [50]. The obtained dilute suspensions (~0.3% by volume) are dispersed in custom made cylindrical glass cuvettes of 6 mm diameter and bottom thickness of ~170 μm (no. 1 coverslips). All measurements are conducted at 20 °C.

A VisiTech 'VT-infinity^3' Confocal Scanning Laser Microscope (CSLM) is used to capture image-time series. The CSLM unit is connected to a Nikon Eclipse Ti-U inverted microscope, a Hamamatsu digital camera (ORCA-flash 4.1, ~100 fps) and a 100 mW 488 nm excitation laser source. A 100 × oil immersion objective with 1.49 numerical aperture is used to capture the images. Z-ranges spanning 6–12 μm are examined, where the lowest focal plane is set at 10 μm above the glass bottom to avoid wall effects on the particle dynamics. Individual Z-stacks (i.e. time points in 3D localization) are captured using 1024 × 1024 pixels (of effective size 67.5 nm) in (X,Y) and 61–121 steps (of 100 nm) along the Z direction. The (per experiment uniform) lag time per Z-stack ranges between 1.7 and 2.7 s. Addressed lag times are in the range where diffusive motion starts to exceed noise levels. Number of time points (i.e. Z-stacks) are ranging between 90 and 168 per sample and the duration of the experiments are up to 408 s.

2.5. Extracting rotation and translation

For optimal visualization, the probes are dispersed in refractive index matching solvent mixtures (n = 1.45). Solvents are water-glycerol (S_1, 1:4 by weight, η = 59 mPa.s) and water-glycerol-Dimethyl sulfoxide (DMSO) (S_2, 2:4:3 by wt., η = 20 mP a.s). Particle volume fractions are chosen around 0.3%, to approach the dilute limit while keeping enough particles in the image volume for obtaining sufficient accuracy. CSLM in fluorescence mode is used to visualize only the labeled berries. Their Cartesian coordinates are extracted using well-known particle locating algorithms [51,52]. The located berries are then grouped in clusters to identify to which raspberry probe they belong; this is achieved using a maximum distance criterion (see SI for details). Only raspberries that contain 4 or more non-coplanar tracers are kept. This minimum number is required for simultaneously finding the center location (x,y,z) and optical radius (R_{fit}) of the raspberry particle, which is achieved via least-squares fitting to a sphere. Each obtained center location then provides an origin in a 3D Cartesian coordinate system that allows defining the spatial orientation of the raspberry probe based on the angular positions of the tracer berries. In this scheme, the translation of each raspberry is extracted from the time-dependent center location, leaving the rotational motion to be measured from the changes in orientation via applying rigid body transformations in between consecutive time steps [37]. The key steps involved in dissecting translational and rotational motion are illustrated in Fig. 2. We have used a modified algorithm, based on Ref. [37], to calculate angular displacements from a rotational transformation matrix in terms of 3 Euler angles.

$$\begin{bmatrix} x_{i+1} \\ y_{i+1} \\ z_{i+1} \end{bmatrix} = \mathbf{R} \begin{bmatrix} x_i \\ y_i \\ z_i \end{bmatrix} \quad (1)$$

where [x, y, z] coordinates denote the location of an individual berry tracer at ith time step and **R** is the rotational transformation

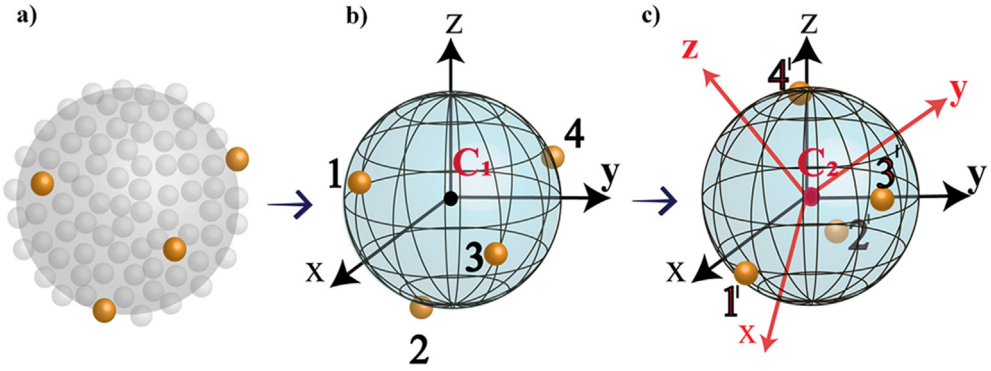

Fig. 2. Key steps in measuring translation and rotation of a raspberry probe: (a) 3D localization of the fluorescent berries, (b) fitting a sphere that encompasses the cluster, (c) tracking the rotational displacement using a frame of reference fitted at the core center.

matrix. The calculation of R is as given in [37]. After obtaining this transformation matrix, we calculate the rotations around each principle axes. A general rotational matrix has the form:

$$\mathbf{R}=\begin{bmatrix} cos\beta cos\gamma & sin\alpha sin\beta cos\gamma - cos\alpha sin\gamma & cos\alpha sin\beta cos\gamma + sin\alpha sin\gamma \\ cos\beta sin\gamma & sin\alpha sin\beta sin\gamma + cos\alpha cos\gamma & cos\alpha sin\beta sin\gamma - sin\alpha cos\gamma \\ -sin\beta & sin\alpha cos\beta & cos\alpha cos\beta \end{bmatrix} \quad (2)$$

where α, β and γ are the rotations around the principal x, y and z axes respectively. This rotation matrix is used to calculate the Euler angles directly [53] (details are given in SI). For particles with spherical symmetry, due to the bounded nature of rotation angles, the calculation of angular displacements relative to the axis of rotation will yield diffusion coefficient greater than a factor of 3/2 of the actual value [37]. For that reason MSAD values are multiplied for a factor of 2/3 before calculating rotational diffusion coefficient using Eq. (4).

Construction of trajectories from the time-dependent coordinates is achieved via publicly available tracking routines [54]. The accuracy of the codes was tested with simulated data (mimicking typical experimental conditions) and gave good agreement (Fig. S3, Supporting Information).

The coupled displacement of a group of berries on a raspberry is illustrated in Fig. 3a for several time steps. Typical rotational and translational trajectories for a raspberry are shown in Fig. 3b and c.

The mean squared displacement (MSD) versus lag time is calculated from the translational trajectories after the usual drift correction based on the ensemble averaged motion of the tracked particles. Hereafter the translational diffusion coefficient D_t is calculated from:

$$\mathrm{MSD} = 6D_t\Delta\tau \quad (3)$$

The mean squared angular displacement (MSAD) is calculated in an analogous manner, but without the need for a drift correction. The rotational diffusion coefficient D_r is obtained from Eq. (4) below:

$$MSAD = 4D_r\Delta\tau \quad (4)$$

2.6. Estimation of noise levels

The uncertainty in localization is estimated by tracking the 3D locations of fluorescent polystyrene particles (r = 0.5 μm) immobilized on the bottom of the cuvettes. The measured (apparent) displacements are given in SI Fig. S4.a. The corresponding MSDs are resulted in noise level of ~2.5×10^{-3} μm^2 (given in Fig. S4.b). The noise floor of the rotational tracking is estimated based on simulated trajectories of non-diffusing probes with 4 fluorescent tracers. Localization errors (taken as [10 10 50] nm for [x y z] coordinates) are introduced in the simulation to mimic the real experimental conditions. The corresponding MSADs are resulted in a noise level of $2x10^{-3}$ rad^2 (given in Fig. S4.c). Resolution of the confocal microscope along the 3 principal axes is estimated by measuring point spread functions along x, y and z axes. Corresponding resolutions are ~270 nm for x and y and 445 nm for z.

3. Results

3.1. Validation of Brownian behavior

We now examine the accuracy of measuring the diffusion coefficients for our raspberry probes, in different stages of the data analysis. First, we consider the fitted sphere's radius (R_{fit}) as extracted from the center locations of its berries. Given the dispersities of the core and berry systems, R_{fit} should be close the sum of the typical radii: $R_{fit} \approx \langle R_{core} \rangle + \langle R_{berry} \rangle$, where the brackets indicate an average. Using transmission electron microscopy (TEM), we find R_{core} = 1041 ± 33 nm and R_{berry} = 160 ± 14 nm. Fig. 4a shows R_{fit} to be peaked at ≈1280 nm, giving a fairly close correspondence. The calculated standard deviation of 35 nm is the resultant of the two polydispersities and the typical uncertainty in R_{fit}, which is estimated to be 44 nm. The larger R_{fit} values (>1.3 μm) are rare, and ascribed to photo-bleaching (after long exposure) which compromises the berry localizations.

For the translational trajectories, the removal of drift is an essential correction, unless the lag time $\tau \ll D_t/v^2$, with v the drift velocity [55]. In our case, drift analysis also contributes to validation, because the vertical motion is dominated by sedimentation. The latter is illustrated in Fig. 4b for a typical probe trajectory. Accordingly, the axial displacement of the ensemble of raspberries shows good linearity, as can be seen in Fig. 4c. Since the particle volume fraction is very low, a comparison can be made between v and theoretical Stokes sedimentation velocity of a smooth sphere. The dashed line in Fig. 4c is a linear fit that encompasses the axial drift displacement signal. Based on the Stokes Law, the effective radius of the corresponding smooth sphere calculated from the linear fit is 1.28 μm which is close to the average TEM radius of the RP. Drift signals in the horizontal directions are ascribed to the translation of microscope stage.

The principal results of this work, obtained after all analysis steps and thus accumulating the inaccuracies of all these steps, are shown in Fig. 4d and e. Here, the solid black lines represent the (drift corrected) MSD and the MSAD respectively. Both functions show a linear dependence on lag time, as expected for pure Brownian motion. The shortest addressed lag time is 2.4 s, as determined by the acquisition time of a 3D confocal scan and the exper-

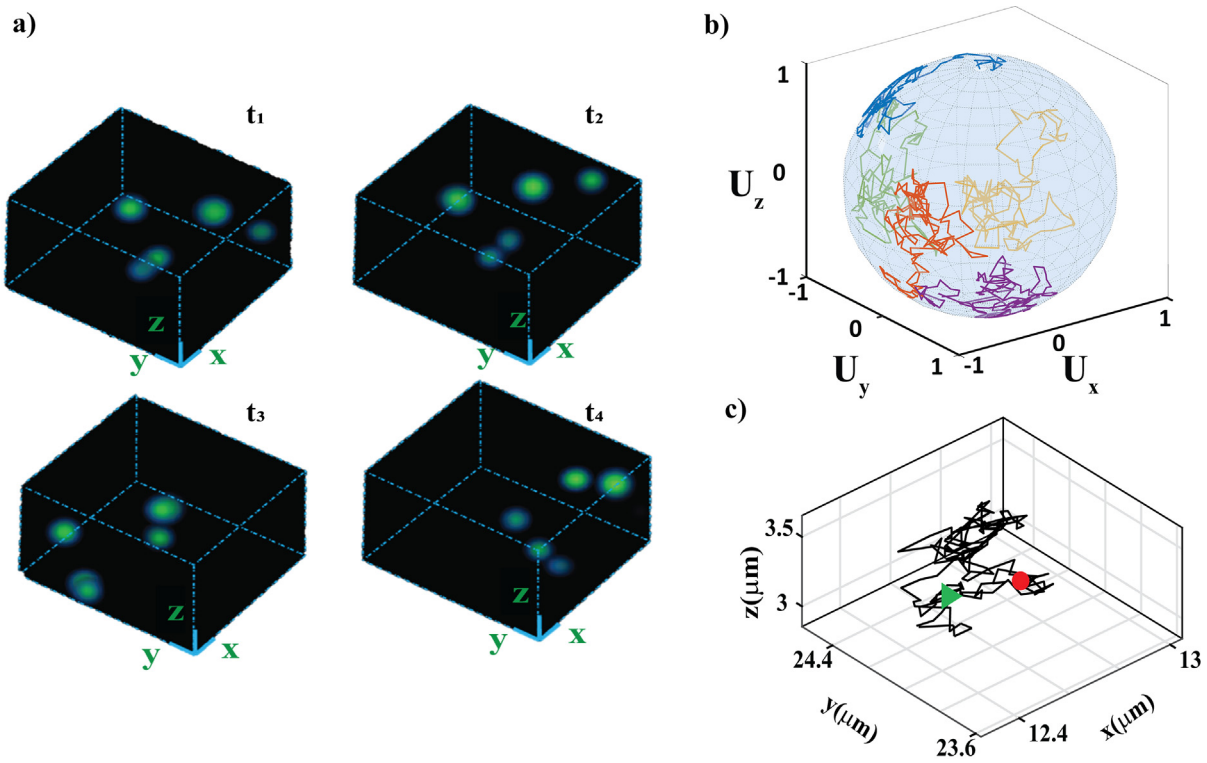

Fig. 3. Visual demonstration of typical results for tracking a single raspberry probe. (a) Coupled motion of fluorescent berry particles forming a cluster at different time steps (3D rendering done with ImageJ FIJI), a movie can be seen in the Supporting Information as S.mov2, (b) Orientational trajectories of the 5 berries (differing in color) projected onto the surface of a unit sphere, (c) Center-of-mass trajectory of a single raspberry particle (green = begin, red = end).

iment duration is 387 s. Both the MSD and the MSAD are significantly above their respective noise floors.

Because of the spherical symmetry of the system, none of the two diffusion coefficients should show any directionality. Decompositions of the MSD and MSAD along the X, Y and Z directions of the lab frame confirm this: the components along the different directions superimpose well in both Fig. 4d and e. Also the displacement histograms for a representative lag time (see insets) show a very good overlap and a Gaussian shape. This further corroborates that both types of diffusive motion are captured well.

3.2. Rotational and translational diffusion coefficients

To assess the accuracy of the measured diffusion coefficients, we compare MSDs and MSADs for the two probe systems (RP, SP) in solvents with different viscosities: S_1 (59 ± 3 mPa.s) and S_2 (20 ± 1 mPa.s). Both probes are synthesized using the same core and berry particles, but for the SP system, a thicker silica layer has been overgrown to achieve a smoothened surface (Fig. 1e). This thicker layer also gives a significant increase in the final probe size (Fig. 5a). The MSAD measurements are shown in Fig. 5b. Regardless of the solvent, both the RP and SP probes demonstrate a purely diffusive behavior, i.e. a linear increase in MSAD with lag time. Extracted numerical data are summarized in Table 1, where the diffusion coefficients are obtained from linear fits for lag times up to 10 s.

In the dilute limit, it is interesting to compare the measured D_r and D_t values to the theoretical expressions for smooth spheres in a Newtonian liquid with a no-slip boundary condition [56]. D_t is given by Stokes-Einstein equation and D_r is given by Stokes-Einstein-Debye equation as follows:

$$D_t = \frac{k_b T}{6\pi\eta R} \tag{5}$$

$$D_r = \frac{k_b T}{8\pi\eta R^3} \tag{6}$$

where k_b is the Boltzmann constant, T is temperature and R is radius. Also for rough spheres, D_r and D_t should be inversely proportional to the solvent viscosity η. Calculating $D_i(S_1)/D_i(S_2)$ with $i \in r, t$ for RP and SP separately, we obtain $\eta(S_1)/\eta(S_2)$ = 3.2 ± 0.3, in good agreement with the 3.0 ± 0.2 obtained from the measured viscosities.

Comparing the cases where the same probe system is dispersed in 2 different solvents, a different accuracy assessment can be made by calculating D_t/D_r. Now the viscosity effect is 'divided out' because of the inverse proportionality of both D_t and D_r to η. The results in Table 1 show very similar ratios (~1.82 ± 0.08 μm^2) for RP and more differing ones (~2.2 ± 0.3 μm^2) for SP. The larger D_t/D_r values for the SP probes are not unexpected, considering the R^2 proportionality for smooth spheres. The small variations among the measurements in different solvents might be due to a 'sampling effect': a combined effect of the poly-dispersity (Fig. 5a) and the finite number of probes (typically 20–30) in a single image volume.

Lastly, we use the standard expressions (Eqs. (5) and (6)) for D_t and D_r of smooth spheres in the dilute limit, to calculate effective radii R_h from the measured diffusion coefficients and solvent viscosities. The R_h values in Table 1 are comparable to those from the TEM measurements (Fig. 5a). Some slight differences between the values obtained from S_1 and S_2 are found; these can be attributed to the fact that each of the 4 raspberry/solvent combinations was explored with a fresh solvent mixture (possibility of slight differences in viscosities) and a limited number of particles (possibly introducing a sampling effect). A striking observation is that for both RP and SP, the R_h values obtained from D_r correspond better with TEM measurements. Considering the R^3 proportionality of D_r for smooth spheres (while it is ~R^{-1} for D_t) it is likely that D_r

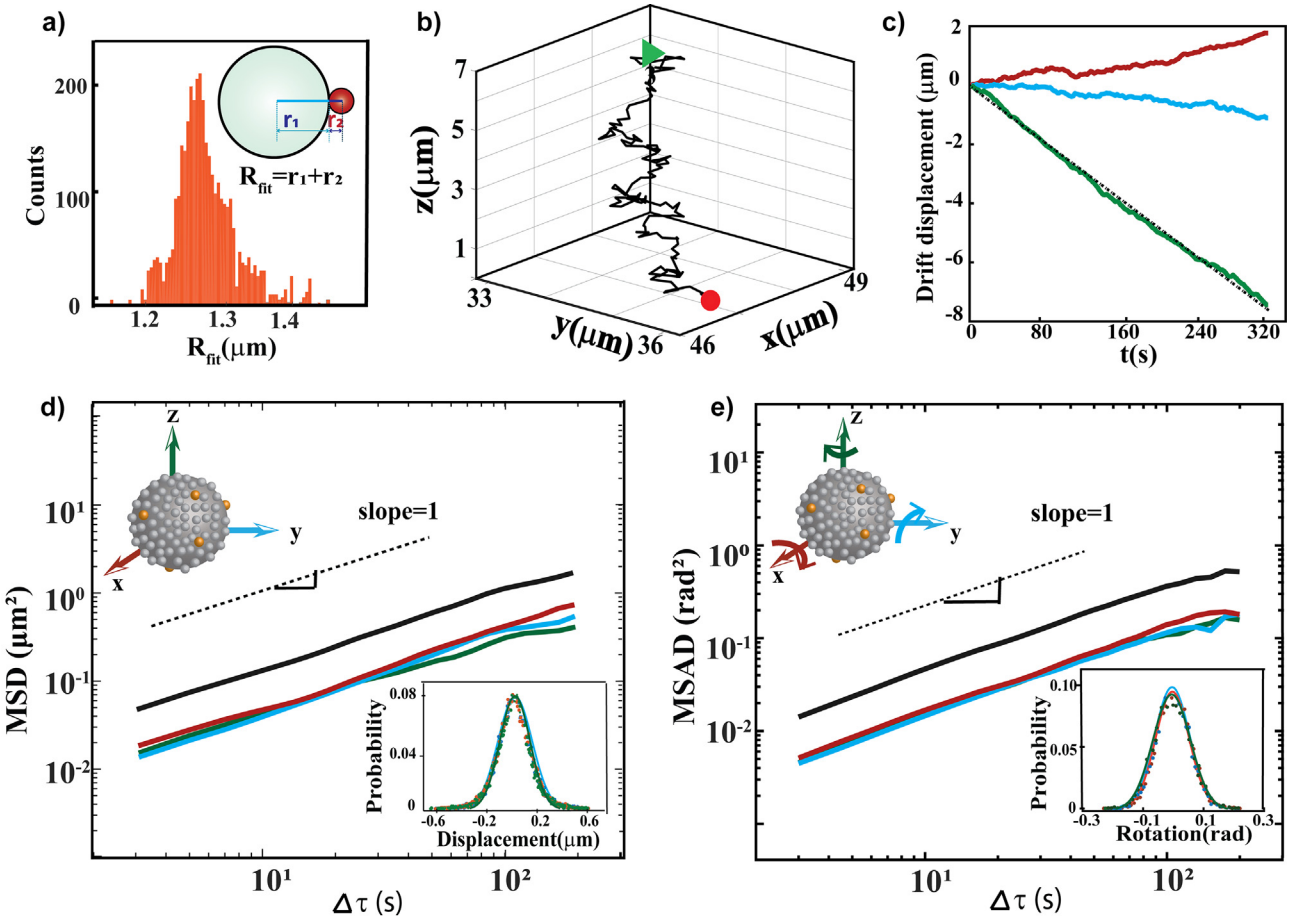

Fig. 4. Key results of translational and rotational tracking. a) Histogram of fitted radius R_{fit} (see inset) for both type of probes (which are optically identical). b) Typical 3D trajectory of a RP, before the removal of drift motion. c) Drift displacements for an ensemble of RP raspberries in solvent S_1, along the x, y and z directions. d) MSD and e) MSAD versus lag time (solid black lines) for RP probes in solvent S_1. Both functions are obtained from the same image data and based on 18 probes. Insets show decompositions along x, y and z for the MS(A)D, and for the displacement histograms. Color coding: red = x, blue = y, green = z.

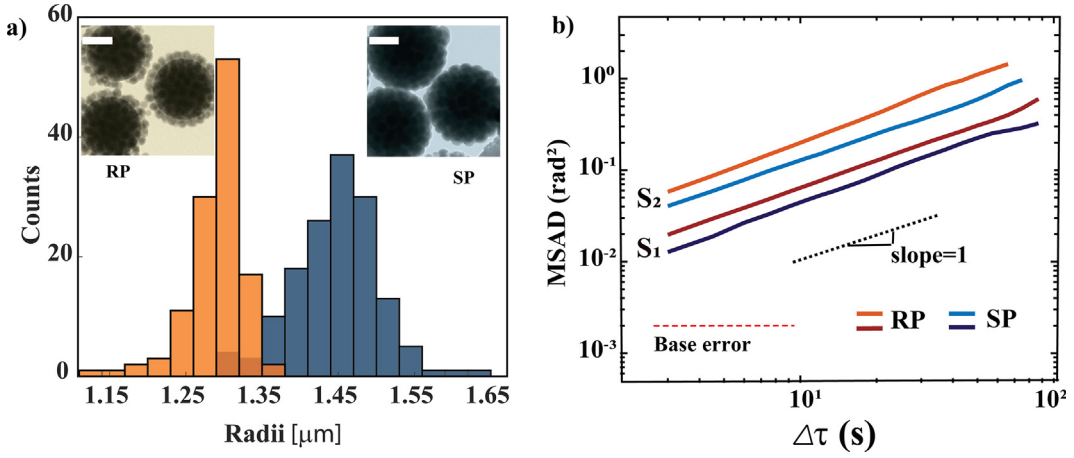

Fig. 5. (a) Size distributions and TEM close-ups for RP (orange) and SP (blue). Scale bar is 1 μm. (b) MSAD versus lag time for raspberry systems RP (orange/brown) and SP (blue/purple) dispersed in solvents S_1 (η = 59 mPa.s) and in S_2 (η = 20 mPa.s).

provides a more precise measure for R_h. Considering how close $\langle R_h [D_t] \rangle$ and $\langle R_h [D_r] \rangle$ are to those of the TEM measurements, we conclude that the surface roughness (being larger for RP) does not have a discernable effect on either of the two diffusion coefficients in the dilute limit.

4. Application scope

Our novel probes could be useful in various cases where simultaneous 3D tracking of individual particle locations and orientations is needed. Due to tunability of the outer layer thickness,

Table 1
Overview of measured diffusion coefficients and some derived quantities. R_h is the hydrodynamic radius of the equivalent smooth sphere.

	D_t ($\mu m^2/s$)	D_r (s^{-1})	D_t/D_r (μm^2)	R_h_[D_t] (μm)	R_h_[D_r] (μm)
RP in S_1	$2.78 \cdot 10^{-3}$	$1.58 \cdot 10^{-3}$	1.76	1.29	1.20
RP in S_2	$9.73 \cdot 10^{-3}$	$5.18 \cdot 10^{-3}$	1.88	1.09	1.15
SP in S_1	$2.23 \cdot 10^{-3}$	$1.13 \cdot 10^{-3}$	1.97	1.61	1.34
SP in S_2	$7.58 \cdot 10^{-3}$	$3.10 \cdot 10^{-3}$	2.45	1.40	1.37

surface roughness can be altered. This offers a broad application potential for our particles in many colloidal dynamics studies. At low particle concentrations the effects of roughness on the two diffusion coefficients were too subtle to be measured. However at high concentrations, rough probes can be employed for studying the relation between roughness and diffusion. In the dense regime, particle-particle interactions play an important role in colloidal dynamics, and strong correlations between roughness and jamming have already been found [57–59]. In the smooth limit, our probes can be used for shedding more light on the effect of colloidal interactions on rotational diffusion [60,61] or on transient phenomena like glassy dynamics and crystallization. Also in complex fluids whose structure is not dictated by particles, our (rough or smooth) probes could provide information about local (mechanical) properties. Here the surrounding 'bulk' material could e.g. be polymer solutions/gels or liquid interfaces.

Lastly, the synthesis and utilization of raspberry probes are not limited to the demonstrated methodology. Due to the simple synthesis and the use of only one fluorescent label for simultaneous tracking of two different motions, the 'berry platform' can pave the way for designing similar probes with additional shape isotropy. To make use of our method, minimum number of tracer berries is 4, but the systems with higher number of fluorescent tracers will also provide accurate results. One design criterion to keep in mind here is, that fluorescent tracers' distances must be larger than the optical resolution. Applying the 'labeled raspberry' concept while using different materials is yet another direction. Probes could also be functionalized as active colloids, soft compressible particles, or serve in biomimicking studies to resolve dynamics of biological processes [19,62].

5. Conclusions

The use of (confocal) microscopy to track translational motion of colloidal spheres has evolved into a broadly applied method in soft matter science in the past two decades. Tracking also the rotation of the spheres is much less common, in spite of the enhanced insights it can offer. This could be related to limitations of existing probes regarding their (non-spherical) shape or (non-uniform) surface chemistry [20]. We developed very-nearly-spherical ('raspberry'), optically anisotropic probes with an all-silica surface. Surface roughness can be controlled via the thickness of the overgrown silica layer. Adding 4 (or more) fluorescent tracers in the shell enables a precise measurement of both the center location and the orientation of the probe. We demonstrated the utility of our probes by measuring 3D translational and rotational diffusion coefficients in different solvents. In the dilute limit, the probes exhibit purely diffusive behavior, with diffusion coefficients that are similar to theoretical values for smooth spheres of the same size. We envision that the concept of 'raspberry'-based rotational-translational probes can be exploited in different directions, for example the use of different materials, and in particular the study of more complex systems having a heterogeneous dynamics.

CRediT authorship contribution statement

Beybin Ilhan: Conceptualization, Methodology, Software, Investigation, Visualization, Formal analysis, Writing - original draft, Writing - review & editing. **Jelle J. Schoppink:** Investigation, Software, Formal analysis. **Frieder Mugele:** Supervision, Writing - review & editing, Resources. **Michael H.G. Duits:** Conceptualization, Supervision, Resources, Writing - review & editing, Funding acquisition, Project administration.

Declaration of Competing Interest

The authors declare that they have no known competing financial interests or personal relationships that could have appeared to influence the work reported in this paper.

Acknowledgements

This work was financially supported by NWO-CW (ECHO grant 712.016.004). We thank Mark Smithers for SEM imaging and Rico Keim for TEM imaging, Joris Sprakel for providing dedrifting Matlab routines, Dirk van den Ende for fruitful discussions.

Appendix A. Supplementary material

Supplementary data to this article can be found online at https://doi.org/10.1016/j.jcis.2020.05.026.

References

[1] T.G. Mason, K. Ganesan, J.H. vanZanten, D. Wirtz, S.C. Kuo, Particle tracking microrheology of complex fluids, Phys. Rev. Lett. 79 (17) (1997) 3282–3285.
[2] D.T. Chen, E.R. Weeks, J.C. Crocker, M.F. Islam, R. Verma, J. Gruber, A.J. Levine, T. C. Lubensky, A.G. Yodh, Rheological microscopy: Local mechanical properties from microrheology, Phys. Rev. Lett. 90 (2003) (10).
[3] T.A. Waigh, Microrheology of complex fluids, Rep. Prog. Phys. 68 (3) (2005) 685–742.
[4] V. Breedveld, D.J. Pine, Microrheology as a tool for high-throughput screening, J. Mater. Sci. 38 (22) (2003) 4461–4470.
[5] A. Yethiraj, A. van Blaaderen, A colloidal model system with an interaction tunable from hard sphere to soft and dipolar, Nature 421 (6922) (2003) 513–517.
[6] W.K. Kegel, A. van Blaaderen, Direct observation of dynamical heterogeneities in colloidal hard-sphere suspensions, Science 287 (5451) (2000) 290–293.
[7] E.R. Weeks, J.C. Crocker, A.C. Levitt, A. Schofield, D.A. Weitz, Three-dimensional direct imaging of structural relaxation near the colloidal glass transition, Science 287 (5453) (2000) 627–631.
[8] P.N. Pusey, W. van Megen, Observation of a glass transition in suspensions of spherical colloidal particles, Phys. Rev. Lett. 59 (18) (1987) 2083–2086.
[9] E.R. Weeks, D.A. Weitz, Properties of cage rearrangements observed near the colloidal glass transition, Phys. Rev. Lett. 89 (9) (2002) 095704.
[10] M.D. Wehrman, A. Leduc, H.E. Callahan, M.S. Mazzeo, M. Schumm, K.M. Schultz, Rheological properties and structure of step- and chain-growth gels concentrated above the overlap concentration, Aiche J. 64 (8) (2018) 3168–3176.
[11] K.M. Schultz, A.D. Baldwin, K.L. Kiick, E.M. Furst, Gelation of covalently Cross-Linked PEG-heparin hydrogels, Macromolecules 42 (14) (2009) 5310–5316.
[12] C.R. Nugent, K.V. Edmond, H.N. Patel, E.R. Weeks, Colloidal glass transition observed in confinement, Phys. Rev. Lett. 99 (2) (2007).
[13] H.B. Eral, J.M. Oh, D. van den Ende, F. Mugele, M.H.G. Duits, Anisotropic and Hindered diffusion of colloidal particles in a closed cylinder, Langmuir 26 (22) (2010) 16722–16729.

[14] H.B. Eral, D. van den Ende, F. Mugele, M.H.G. Duits, Influence of confinement by smooth and rough walls on particle dynamics in dense hard-sphere suspensions, Phys. Rev. E 80 (6) (2009).
[15] S. Ghosh, D. Wijnperle, F. Mugele, M.H.G. Duits, Dynamics of colloids confined in microcylinders, Soft Matter 12 (5) (2016) 1621–1630.
[16] T. Moschakis, Microrheology and particle tracking in food gels and emulsions, Curr. Opin. Colloid Interface Sci. 18 (4) (2013) 311–323.
[17] M.H.G. Duits, Y.X. Li, S.A. Vanapalli, F. Mugele, Mapping of spatiotemporal heterogeneous particle dynamics in living cells, Phys. Rev. E 79 (5) (2009).
[18] J.C. Crocker, B.D. Hoffman, Multiple-particle tracking and two-point microrheology in cells, Cell Mech. 83 (2007) 141–178.
[19] S.-L. Liu, Z.-L. Zhang, Z.-Q. Tian, H.-S. Zhao, H. Liu, E.-Z. Sun, G.F. Xiao, W. Zhang, H.-Z. Wang, D.-W. Pang, Effectively and efficiently dissecting the infection of influenza virus by quantum-dot-based single-particle tracking, ACS Nano 6 (1) (2012) 141–150.
[20] S.M. Anthony, Y. Yu, Tracking single particle rotation: probing dynamics in four dimensions, Anal. Methods 7 (17) (2015) 7020–7028.
[21] M. Kim, S.M. Anthony, S.C. Bae, S. Granick, Colloidal rotation near the colloidal glass transition, J. Chem. Phys. 135 (5) (2011) 054905.
[22] M.D. Ediger, Spatially heterogeneous dynamics in supercooled liquids, Annu. Rev. Phys. Chem. 51 (1) (2000) 99–128.
[23] S. Schütter, J. Roller, A. Kick, J.-M. Meijer, A. Zumbusch, Real-space imaging of translational and rotational dynamics of hard spheres from the fluid to the crystal, Soft Matter 13 (44) (2017) 8240–8249.
[24] G. Boniello, C. Blanc, D. Fedorenko, M. Medfai, N.B. Mbarek, M. In, M. Gross, A. Stocco, M. Nobili, Brownian diffusion of a partially wetted colloid, Nat. Mater. 14 (9) (2015) 908–911.
[25] A. Stocco, B. Chollet, X. Wang, C. Blanc, M. Nobili, Rotational diffusion of partially wetted colloids at fluid interfaces, J. Colloid Interface Sci. 542 (2019) 363–369.
[26] S.W. Chee, U. Anand, G. Bisht, S.F. Tan, U. Mirsaidov, Direct observations of the rotation and translation of anisotropic nanoparticles adsorbed at a liquid-solid interface, Nano Lett. 19 (5) (2019) 2871–2878.
[27] P. Kukura, H. Ewers, C. Müller, A. Renn, A. Helenius, V. Sandoghdar, High-speed nanoscopic tracking of the position and orientation of a single virus, Nat. Methods 6 (12) (2009) 923.
[28] B.W.M. Kuipers, M.C.A. van de Ven, R.J. Baars, A.P. Philipse, Simultaneous measurement of rotational and translational diffusion of anisotropic colloids with a new integrated setup for fluorescence recovery after photobleaching, J. Phys.-Condens. Matter 24 (24) (2012).
[29] M.P. Lettinga, G.H. Koenderink, B.W.M. Kuipers, E. Bessels, A.P. Philipse, Rotational dynamics of colloidal spheres probed with fluorescence recovery after photobleaching, J. Chem. Phys. 120 (9) (2004) 4517–4529.
[30] G.H. Koenderink, A.P. Philipse, Rotational and translational self-diffusion in colloidal sphere suspensions and the applicability of generalized Stokes-Einstein relations, Langmuir 16 (13) (2000) 5631–5638.
[31] Y. Wang, C. Li, G.J. Pielak, Effects of proteins on protein diffusion, J. Am. Chem. Soc. 132 (27) (2010) 9392–9397.
[32] H. Sun, Z. Wang, Y. He, Direct observation of spatiotemporal heterogeneous gelation by rotational tracking of a single anisotropic nanoprobe, ACS Nano 13 (10) (2019) 11334–11342.
[33] Z. Cheng, T. Mason, Rotational diffusion microrheology, Phys. Rev. Lett. 90 (1) (2003) 018304.
[34] Y. Peng, L. Lai, Y.-S. Tai, K. Zhang, X. Xu, X. Cheng, Diffusion of ellipsoids in bacterial suspensions, Phys. Rev. Lett. 116 (6) (2016) 068303.
[35] J. Roller, P. Pfleiderer, J.-M. Meijer, A. Zumbusch, Detection and tracking of anisotropic core-shell colloids, J. Phys.: Condens. Matter 30 (39) (2018) 395903.
[36] M. Hoffmann, C.S. Wagner, L. Harnau, A. Wittemann, 3D Brownian diffusion of submicron-sized particle clusters, ACS Nano 3 (10) (2009) 3326–3334.
[37] G.L. Hunter, K.V. Edmond, M.T. Elsesser, E.R. Weeks, Tracking rotational diffusion of colloidal clusters, Opt. Express 19 (18) (2011) 17189–17202.
[38] S.M. Anthony, M. Kim, S. Granick, Translation-rotation decoupling of colloidal clusters of various symmetries, J. Chem. Phys. 129 (24) (2008) 244701.
[39] T. Besseling, M. Hermes, A. Kuijk, B. De Nijs, T. Deng, M. Dijkstra, A. Imhof, A. Van Blaaderen, Determination of the positions and orientations of concentrated rod-like colloids from 3D microscopy data, J. Phys.: Condens. Matter 27 (19) (2015) 194109.
[40] J.R. Gomez-Solano, A. Blokhuis, C. Bechinger, Dynamics of self-propelled Janus particles in viscoelastic fluids, Phys. Rev. Lett. 116 (13) (2016) 138301.
[41] S.M. Anthony, M. Kim, S. Granick, Single-particle tracking of janus colloids in close proximity, Langmuir 24 (13) (2008) 6557–6561.
[42] S. Jiang, Q. Chen, M. Tripathy, E. Luijten, K.S. Schweizer, S. Granick, Janus particle synthesis and assembly, Adv. Mater. 22 (10) (2010) 1060–1071.
[43] B. Liu, A. Böker, Measuring rotational diffusion of colloidal spheres with confocal microscopy, Soft Matter 12 (28) (2016) 6033–6037.
[44] W. Stöber, A. Fink, E. Bohn, Controlled growth of monodisperse silica spheres in the micron size range, J. Colloid Interface Sci. 26 (1) (1968) 62–69.
[45] G. Bogush, M. Tracy, C. Zukoski Iv, Preparation of monodisperse silica particles: control of size and mass fraction, J. Non-Cryst. Solids 104 (1) (1988) 95–106.
[46] M. Zanini, C.-P. Hsu, T. Magrini, E. Marini, L. Isa, Fabrication of rough colloids by heteroaggregation, Colloids Surf., A 532 (2017) 116–124.
[47] A. Van Blaaderen, J. Van Geest, A. Vrij, Monodisperse colloidal silica spheres from tetraalkoxysilanes: particle formation and growth mechanism, J. Colioid Interface Sci. 154 (2) (1992) 481–501.
[48] S.D. Coenen, C. De Kruif, Synthesis and growth of colloidal silica particles, J. Colloid Interface Sci. 124 (1) (1988) 104–110.
[49] B. Ilhan, C. Annink, D. Nguyen, F. Mugele, I. Sîretanu, M.H. Duits, A method for reversible control over nano-roughness of colloidal particles, Colloids Surf., A 560 (2019) 50–58.
[50] S. Ghosh, F. Mugele, M.H. Duits, Effects of shear and walls on the diffusion of colloids in microchannels, Phys. Rev. E 91 (5) (2015) 052305.
[51] Y. Gao, M.L. Kilfoi, Accurate detection and complete tracking of large populations of features in three dimensions, Opt. Express 17 (6) (2009) 4685–4704.
[52] K.E. Jensen, N. Nakamura, Note: An iterative algorithm to improve colloidal particle locating, Rev. Sci. Instrum. 87 (6) (2016) 066103.
[53] G.G. Slabaugh, Computing Euler angles from a rotation matrix, Retrieved on August 1999 6 (2000) 39–63.
[54] J.C. Crocker, E.R. Weeks, Particle tracking using IDL, 2011. Retrieved from http://www.physics.emory.edu/faculty/weeks//idl.
[55] M.H. Duits, S. Ghosh, F. Mugele, Measuring advection and diffusion of colloids in shear flow, Langmuir 31 (21) (2015) 5689–5700.
[56] A.P. Philipse, Brownian Motion, Springer, 2018.
[57] C.P. Hsu, S.N. Ramakrishna, M. Zanini, N.D. Spencer, L. Isa, Roughness-dependent tribology effects on discontinuous shear thickening, P. Natl. Acad. Sci. USA 115 (20) (2018) 5117–5122.
[58] L.C. Hsiao, S. Jamali, E. Glynos, P.F. Green, R.G. Larson, M.J. Solomon, Rheological state diagrams for rough colloids in shear flow, Phys. Rev. Lett. 119 (15) (2017).
[59] L.C. Hsiao, I. Saha-Dalal, R.G. Larson, M.J. Solomon, Translational and rotational dynamics in dense suspensions of smooth and rough colloids, Soft Matter 13 (48) (2017) 9229–9236.
[60] G.H. Koenderink, H.Y. Zhang, D. Aarts, M.P. Lettinga, A.P. Philipse, G. Nagele, On the validity of Stokes-Einstein-Debye relations for rotational diffusion in colloidal suspensions, Faraday Discuss. 123 (2003) 335–354.
[61] G.H. Koenderink, M.P. Lettinga, A.P. Philipse, Rotational dynamics of charged colloidal spheres: Role of particle interactions, J. Chem. Phys. 117 (16) (2002) 7751–7764.
[62] K. Welsher, H. Yang, Multi-resolution 3D visualization of the early stages of cellular uptake of peptide-coated nanoparticles, Nat. Nanotechnol. 9 (3) (2014) 198.